ADVANCED MATERIALS TECHNOLOGIES
www.advmattechnol.de

Shape Dependent Conformable Holographic Metasurfaces

*Jianling Xiao, Robert I. Hunter, Duncan A. Robertson, Graham M. Smith, Simon Horsley, Sebastian A. Schulz, and Andrea Di Falco**

In this paper, the design, fabrication, and experimental demonstration of conformable holographic metasurfaces are reported. Here, it is shown that the produced holographic image changes as the metasurface is applied to targets with different shapes. The demonstration is based on a reflective type metasurface, where the reflected polarization is perpendicular to that of the incident light. In addition, how the parameters of the metasurface determine the quality of the images produced and the ability to produce independent images are discussed critically.

1. Introduction

Electromagnetic metasurfaces are engineered 2D materials made by arranging subwavelength[1,2] "meta-atoms" on a surface. Metasurfaces can be designed for applications in different wavelength ranges, from the ultraviolet (UV) to the microwave region.[3–7] Metasurfaces offer unprecedented control over light scattering, including phase, amplitude, and polarization, making them excellent candidates for applications including beam steering,[8–10] optical tweezers,[11] holography,[12–17] lenses and wearable glasses,[18–22] WiFi signal enhancement,[23] and data encryption.[24–26] One of the most successful applications of metasurfaces is in holography, since computer generated holograms can be easily implemented using metasurface technology, where each meta-atom is a pixel of the holographic waveplate. Holographic metasurfaces are particularly well suited to encoding different images into a single design, for example, by multiplexing the incident angles,[27–29] polarizations,[30–32] angular momentum,[33–35] helicity,[36–38] wavelengths,[39,40] and surrounding medium.[41–43] In addition, realizing metasurfaces on flexible substrates is a good way to find practical applications in the real world as they can be conformed to non-flat objects, also in the visible range.[44,45] Their optical response can be coupled[45] or decoupled[46] to their geometrical form, depending on whether the application requires robustness or sensitivity with respect to the shape that they assume. This offers the possibility to multiplex information on to the shape of the metasurface, creating adaptive elements, for example for reconfigurable antennas, photonic skin, or signature control. While previous works have controlled the response of metasurfaces via stretching,[47,48] true shape-multiplexing has not yet been demonstrated. In this paper, we present the design, fabrication, and characterization of conformable metasurfaces which display different holographic images depending on their curvature, as sketched in **Figure 1**.

In the following, we first present our design approach for the multiplexed holograms and for the metasurfaces. We then describe the experimental setup and present and discuss the results. The practical demonstration of our approach was done in the W-band (94 GHz), bending the metasurfaces into cylindrical shapes with opposite curvatures, in reflection configuration as exemplified in Figure 1. For the sake of clarity, the incident light is not shown. It should be noted that our design approach could be readily extended to other frequency domains, albeit with some caveats discussed below.

2. Design and Multiplexing of Holograms

The phase-only holograms were designed using the Gerchberg–Saxton algorithm[49] with the Rayleigh–Sommerfeld[50,51] propagator to model the propagation of light between the metasurface plane and the holographic image plane. To take into account the shape of the beam, we used a Gaussian beam as the source profile, with a beam waist of 2 cm. The intensity profile of the collimated incident beam is shown as Figure S1a, Supporting Information.

To encode two images with different curvatures into one design, we calculated the independent holograms for the two different curvatures and interleaved the resulting phase profiles, as illustrated in **Figure 2**. Figure 2a,d shows the two independent target images to be obtained when the metasurface assumes the convex and concave cylindrical shape curvatures in Figure 2b,e, with radius of curvature $R1 = 35$ mm and $R2 = -100$ mm, respectively. R is defined as the radius of a circle that fits the sample holder, and + and – are used to distinguish

J. Xiao, R. I. Hunter, D. A. Robertson, G. M. Smith, S. A. Schulz, A. D. Falco
School of Physics and Astronomy
University of St Andrews
North Haugh, St Andrews KY16 9SS, UK
E-mail: adf10@st-andrews.ac.uk
S. Horsley
Department of Physics and Astronomy
University of Exeter
Stocker Road, Exeter EX4 4QL, UK
The ORCID identification number(s) for the author(s) of this article can be found under https://doi.org/10.1002/admt.202202006.

DOI: 10.1002/admt.202202006

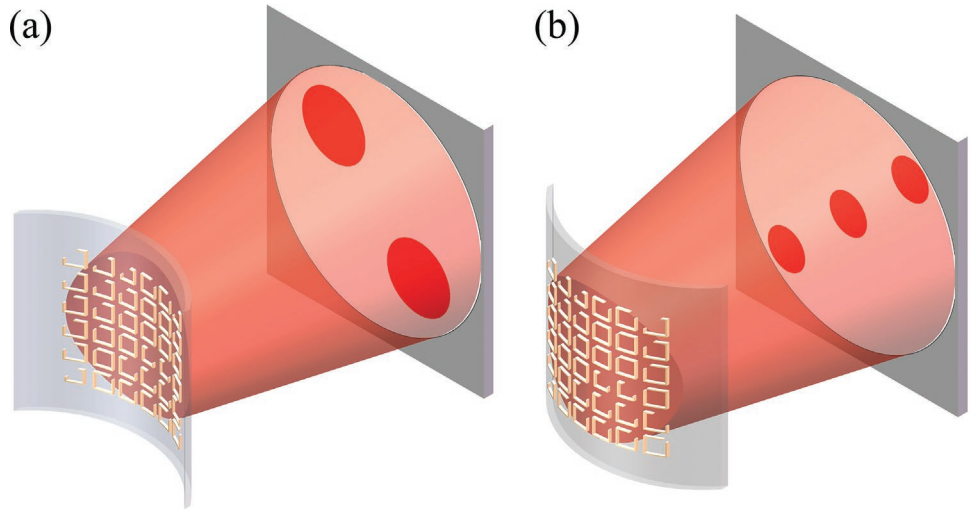

Figure 1. Concept of curvature-dependent multiplexed metasurfaces.

the cylindrical shape associated with convex and concave curvatures. Figure 2c,f shows the individual phase distributions for the target images, which are interleaved in a checkerboard arrangement, to produce a single multiplexed phase distribution, shown in Figure 2g. Each metasurface is made by $N \times N$ square pixels of side $P = 800$ µm, arranged in a square matrix, with $N = 80$, thus with a total size of 64 mm × 64 mm. The size of the pixels was dictated by the wavelength used, whereas N was limited by the spatial dimension of the collimated beam, as further discussed below. The holograms were designed to produce images of 100 cm^2, at an image plane 160 mm from the farthest point of the curved metasurface. These parameters were also chosen to satisfy the experimental constraints.

The reflective holographic metasurfaces were designed to work at 94 GHz ($\lambda = 3.19$ mm) using a popular three-layer scheme to achieve high conversion efficiency, where suitable meta-atoms are separated by a dielectric layer from a reflective surface. Here, the dielectric layer was a flexible polymethyl methacrylate (PMMA) film sandwiched by copper c-rings on top and a reflective copper layer on the bottom. The unit cell of the metasurface is shown in **Figure 3**a. The thickness of PMMA (Tp) and top/bottom copper film (Tc) are 380 µm and 200 nm, respectively and P is the period of the unit cell. The length (L), width (W), and cut-out length (D) of the c-ring structures were chosen pixel-by-pixel to create the required phase shift in the reflected beam. Here, the incident beam is polarized in the horizontal direction (X) whereas the reflected beam from the hologram is polarized in the vertical direction (Y). This allows easy duplexing using a wire grid polarizer for characterization. The response of the meta-atoms was modeled using CST Studio Suite, with the parameter space determined by the fabrication constraints (see next section). In the simulations, we applied unit cell conditions and open boundary conditions along the X/Y and Z-axis, respectively. The electrical conductivity and

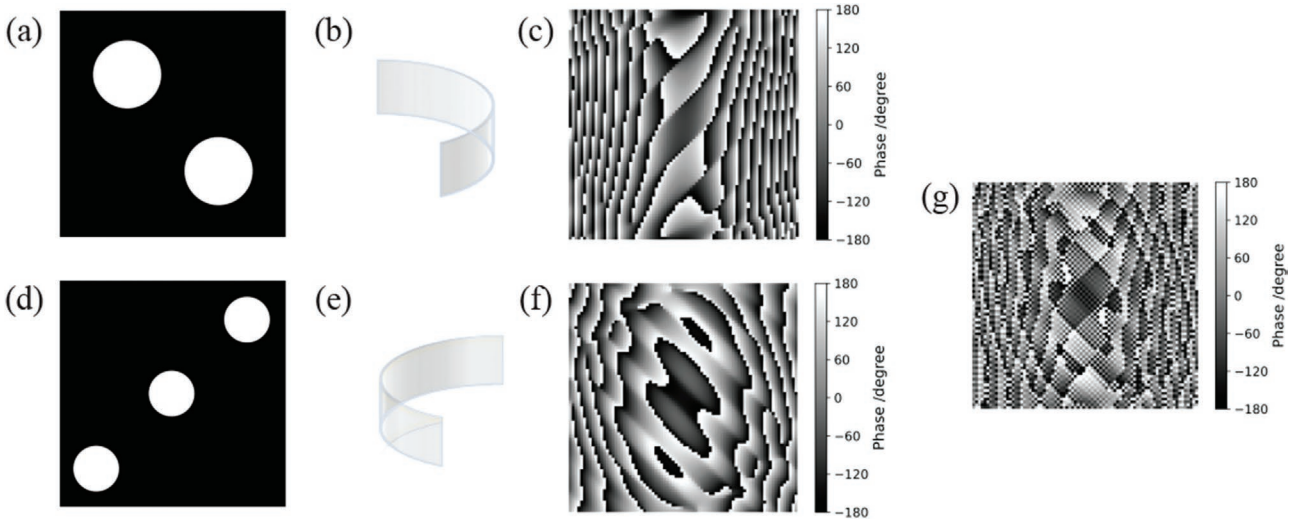

Figure 2. Illustration of the individual and interleaved hologram design. a,d) The independent target images for b) convex and e) concave shapes, where the radius of curvature $R1 = 35$ mm and $R2 = -100$ mm, respectively. c,f) The individual phase distributions for these two target images. g) The interleaved phase distribution of (c) and (f), in a checkerboard arrangement.

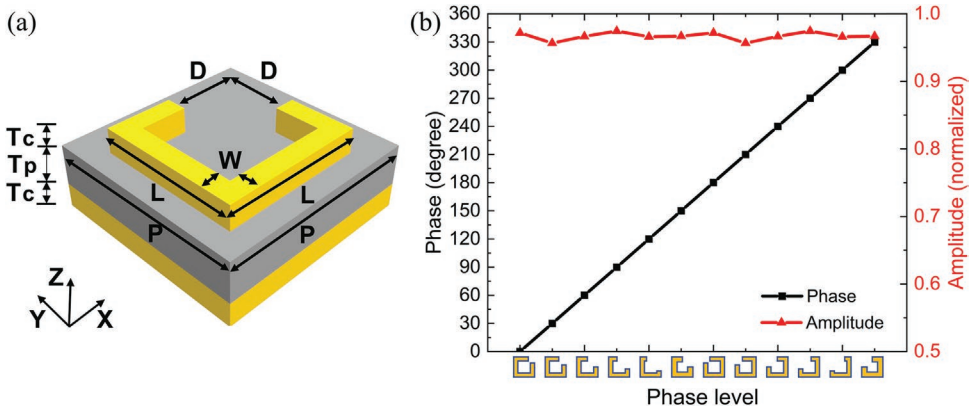

Figure 3. a) Unit cell of c-ring structure. b) Simulated phase shift and normalized amplitude of c-rings at $\lambda = 3.19$ mm, where the thickness and period of spacer layer of PMMA are 380 and 800 µm. The thickness of top and bottom copper layer is 200 nm.

permeability of copper was taken from the CST library with values of $5.96 \times \sim 10^7$ S m^{-1} and 1. The permittivity of the commercially obtained PMMA was measured using a vector network analyzer at W-band (75–110 GHz), which for the used wavelength gave the value $\varepsilon = 2.675 + 0.02i$.

We then designed 12 distinct meta-atoms to cover the phase of reflected light in the [0°, 360°] range, with increments of 30°, as shown in Figure 3b, while maintaining the reflected normalized amplitude at around 0.97. We note that the phase delay caused by the c-rings is based on geometric resonances. Therefore, it is only required to obtain designs for the [0°, 180°] range and the designs for the [180°, 360°] range are obtained by mirroring the meta-atoms through the *Y*-axis. The geometrical parameters of the c-rings for phases in the [0°, 180°] range are supplied in Table S1, Supporting Information.

The modeling of the phase shifts assumes that the meta-atoms are perpendicular to the incident and reflected light, but this can become a significant approximation for metasurfaces with strong local distortion. We therefore investigated the dependence between the phase shift/amplitude and the angle between the meta-atoms and the incident light, producing the results shown in **Figure 4**a,b. For the sake of simplicity, we only explored the effect of tilting around the *Y*-axis, which is most relevant to the cylindrical deformations of the metasurfaces described in this work. The phase delay and normalized amplitude were simulated for the six designs in Table 1, which are designed to cover the phase shift from 0° to 180° when the incident light was in the normal direction. Here we note the incident angle to be 0° for normal incidence. From Figure 4, it can be concluded that our designs show a very good tolerance for incident angles from 0° to 30°, which is comparable with the range covered in our experiments. For practical purposes, we then adopted the response of the meta-atoms as probed at normal incidence. For shapes with local orientation at greater angles respect to the incident light, it would be possible to use a look up table to choose the best meta-atom for the required phase shift. Additionally, it should be noted that since the minimum radius of curvature is more than 40 times larger than the unit cell, the effective change in size of the meta-atoms in the curved configuration can be ignored.

3. Fabrication

A schematic of the photolithographic fabrication process is shown in **Figure 5**. A sheet of PMMA was cut into the desired

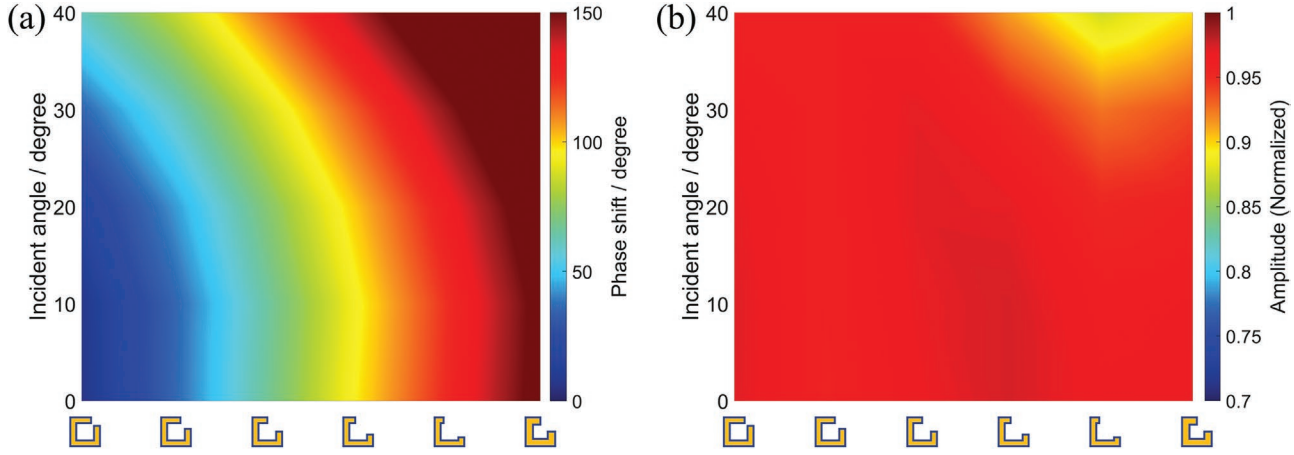

Figure 4. The dependence of six c-ring designs between the a) incident angle and phase shift. b) Incident angle and normalized amplitude. Incident angle is varied away from normal incidence from 0° to 40°.

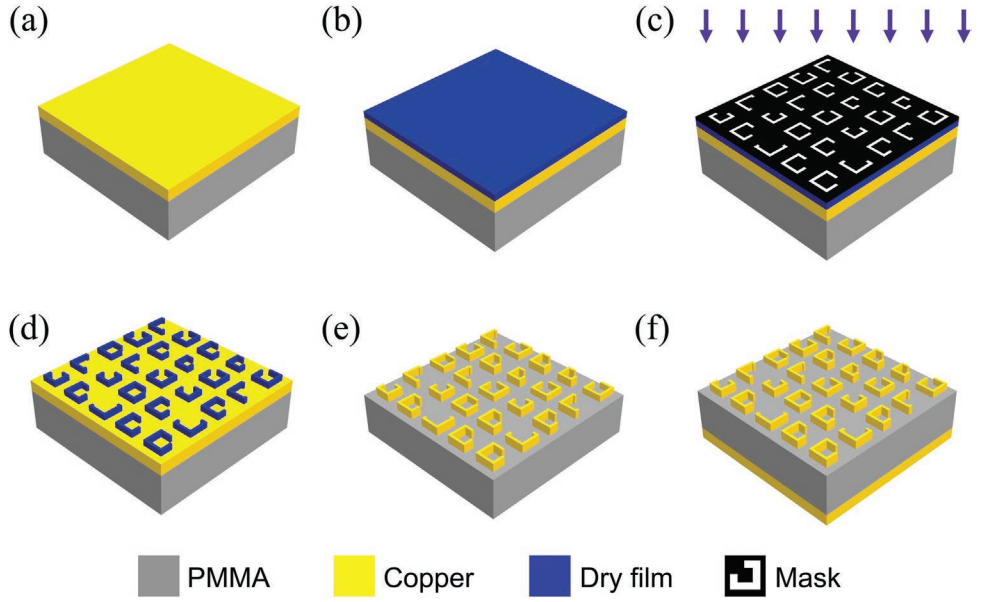

Figure 5. Sketch of the fabrication process. a) A 200 nm thick copper layer is deposited on the PMMA film. b) Dry film is laminated on the top copper layer. C-rings are defined followed by c) UV lithography with a pre-prepared photo mask, d) development, and e) wet-etching with iron chloride solvent. f) A 200 nm copper layer is deposited on the bottom of PMMA film.

size and cleaned with an ultrasonic bath in isopropanol alcohol for 10 min. The sample was then placed in an oven at 90 °C for 4 h to reflow the surface and remove most of the scratches on the surfaces of the PMMA. A 200 nm thick copper layer was then deposited on the top face of the film via electron beam evaporation and laminated with a 20 µm thick negative dry resist (ORDYL Alpha 920). A photomask with c-ring meta-atoms was written with a photoplotter (FilmStar-Plus FP25000) and used to define the metasurface on the film with a 25 s UV exposure using a large format UV exposure unit (UV-AY3623). The exposed sample was then developed with 1% potassium carbonate for 40 s. The patterns were transferred on to the copper via chemical etching, based on an iron chloride solution (2 g : 100 g deionized water) for 2 min. Finally, a 200 nm thick copper layer was deposited on the bottom of sample to form the back reflective layer.

Figure 6a is the image of a fabricated sample and Figure 6b shows a zoomed-in-view of its surface, with a single c-ring in the inset. The quality of the copper features is limited by the use of the dry film. We performed an extensive optimization procedure, for the mask fabrication, exposure, and copper etching, to improve the roughness of the meta-atoms, which could be defined with an accuracy of 10% with respect to the design. The accuracy is calculated as the percentage difference of width and length between the fabricated sample and the target design. While this figure of merit could easily be improved by using a wet photoresist, for example, via spinning or spray coating, it was our intention to demonstrate the viability of a fabrication approach which could more easily be implemented using a roll-to-roll architecture.

The fabricated metasurface was mounted for characterization on either a concave (radius of curvature $R2 = -100$ mm) or convex (radius of curvature $R1 = 35$ mm) sample holder, as shown in panels (c,d) of Figure 6.

4. Results and Discussion

A schematic image of the set-up is shown in **Figure 7**. A Gunn oscillator, with a variable attenuator for power control, was used as the source for the 94 GHz transmitted signal. This signal was coupled to free space via a corrugated feedhorn. The output from this transmitter is linearly polarized and the transmitter was aligned such that this linear polarization was oriented at an angle of +45° with respect to vertical polarization. A suitable lens was used to collimate the beam, producing a Gaussian profiled beam with a 2 cm beam waist at the plane of the metasurface under test. After the lens, the beam passed through a –45° wire grid polarizer (P1) to remove any unwanted cross-polarized signal introduced by the lens before passing through a quasi-optical Faraday rotator (QOFR) which rotated the linear polarization plane to being horizontally polarized for illumination of the metasurface. The QOFR was being used in the set-up as an optical isolator to avoid any reflections back into the transmitter. With the QOFR in place, any horizontally polarized signals returning to the QOFR from the metasurface were further rotated by 45° and these signals were then reflected by P1 into a beam dump made of radar absorbing material (RAM). After the QOFR, the horizontally polarized transmitted signal was reflected by a horizontal wire grid polarizer (P2) on to the metasurface. As discussed in Section 2, the beam reflected from the metasurface was vertically polarized and passed through P2 to the plane where the image was formed, 160 mm from the metasurface. A beam scanner (BS), consisting of a heterodyne receiver coupled to an open waveguide antenna mounted on a motorized stage, that can cover a scan area of 10 cm × 10 cm, was used to record the image by measuring the reflected power at each pixel across the image plane. (It should be noted that the RAM positioned around P1 and P2 used for absorbing unwanted stray beams has been omitted from Figure 7 for clarity.)

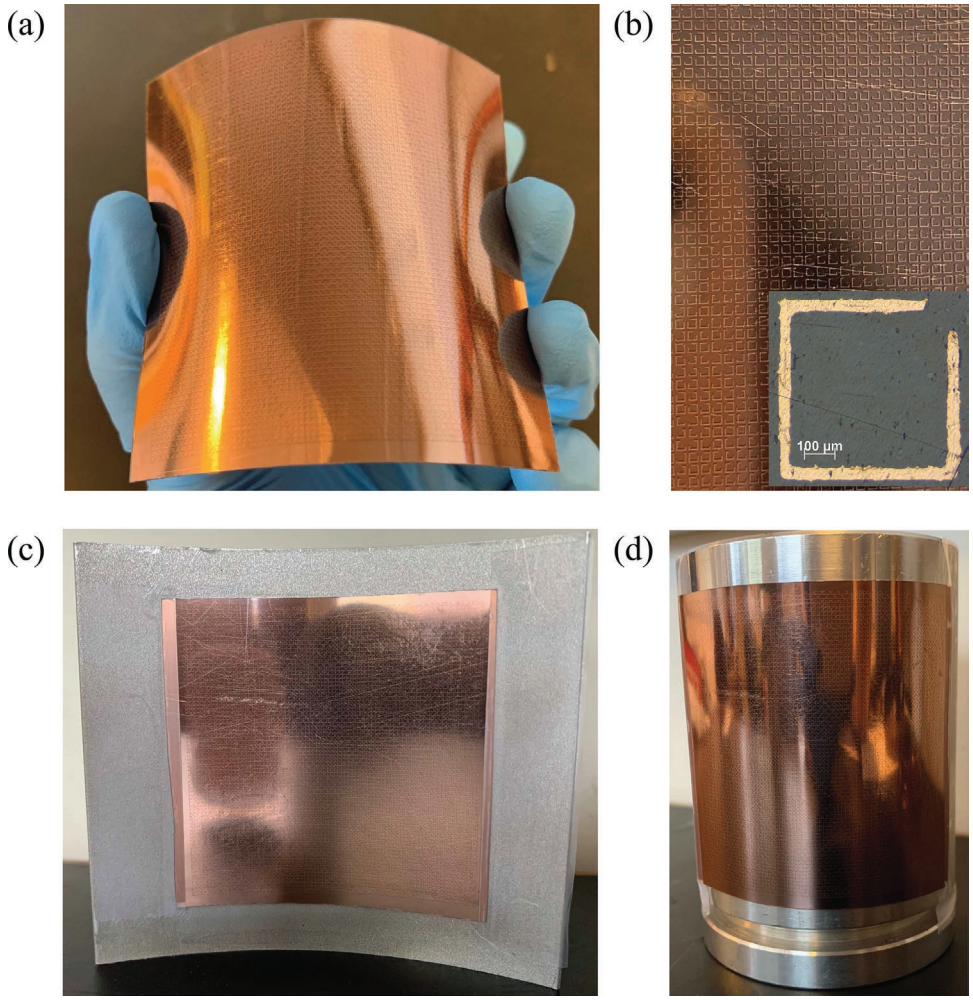

Figure 6. a) Image of a fabricated sample. b) Zoomed-in-view of the sample surface with a single c-ring in the inset. Panels (c) and (d) show the metasurface mounted on the concave ($R2 = -100$ mm) and convex ($R1 = 35$ mm) sample holders, respectively.

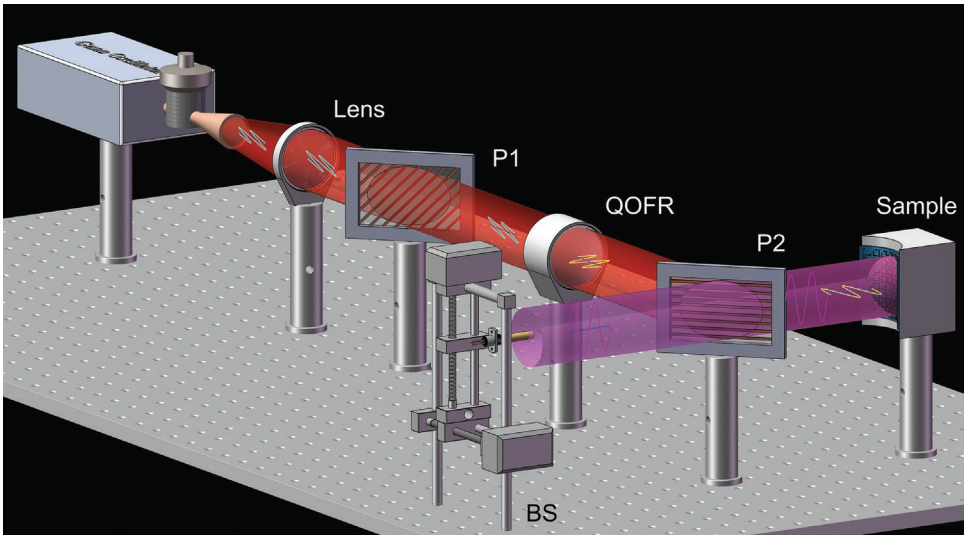

Figure 7. Schematic image of the set-up. The signal is transmitted from the Gunn oscillator and then passes through the lens, –45° wire grid polarizer (P1), quasi-optical Faraday rotator (QOFR) and is reflected by a horizontal wire grid polarizer (P2) on to the metasurface sample. The reflected beam from the metasurface, now with the orthogonal polarization, passes though P2 and is detected by the beam scanner (BS).

The characterization of the multiplexed hologram and the comparison with the simulation are shown in **Figure 8**, where Figure 8a,c shows the simulation results showing two dots and three dots when the curvature of the substrate is bent to $R1 = 35$ mm and $R2 = -100$ mm, and Figure 8b,d are the corresponding experimental results. The numerical images are normalized to the maximum value and plotted in dB with the scale bar range from 0 to −6 dB. The experimental images are normalized to the peak power (−40.5 dBm), after filtering the high frequency noise components and plotted in same scale bar and units with simulations. Figure 8 shows that the experiments fit well with the simulations. The low level noise in the experimental images can be attributed to the fact that the amplitude of the signal of the holographic image is approaching the measurement noise floor (see also Figure S1, Supporting Information). We attribute the differences between the experimental and numerical holographic images to minor fabrication errors. We did notice that the quality of the experimental images also depends strongly on the precise alignment of the set-up, due to the fact that the source beam and the metasurface have comparable size.

The maximum power of the raw holographic image is around −40 dBm (see Figure S1b,c, Supporting Information), whereas the input beam has a maximum of −20 dBm (see Figure S1a, Supporting Information). For reference, the typical maximum power measured for similar metasurfaces when encoding a single image, for a given curvature, is in the range of −30 dBm (see Figure S1d, Supporting Information), which is an example holographic image realized by a metasurface for convex design with the radius of curvature $R = 35$ mm. The reduction in efficiency is a straightforward consequence of the multiplexing, since only half of the available pixels are used for each image, in the multiplexed case. We did not observe any change in the performance of our devices after multiple bending cycles (not shown). This agrees with previous results which show that the optical properties of stacks of PMMA and thin metals do not change even after several thousand bending cycles.[52]

The results of Figure 8 show that we can encode two unrelated images for simple cylindrical curvature. It is useful to consider how many degrees of freedom the platform offers in terms of tunability.

The first thing to consider is that the phase shift with respect to the flat case is due to a displacement of the membrane in the z-direction. For the sake of simplicity, as discussed above, we will assume in the following that the phase shift of the meta-atoms does not change for tilting of +/− 30°. This corresponds to assuming that each meta-atom is perpendicular to the z-axis. In this scenario, two meta-atoms will produce a relative phase shift of 360° if they are displaced along z by a distance equal to the wavelength. Therefore, the number of different phase profiles depends on the conformability of the metasurface substrate. Neglecting stretching effects of the substrate, it would be possible to address independently the phase of each pixel if the substrate could be conformed with features of aspect ratio P:λ (roughly 1:4, in this specific case), which is not a very demanding constraint, even for relatively thick polymeric substrates. In this scenario, the number of degrees of freedom to multiplex information in the metasurface, scales with the number of meta-atoms.

At the wavelength used in this demonstration, a metasurface of $N \times N$ pixels, with area of 1 m^2 would have $N = 1250$.

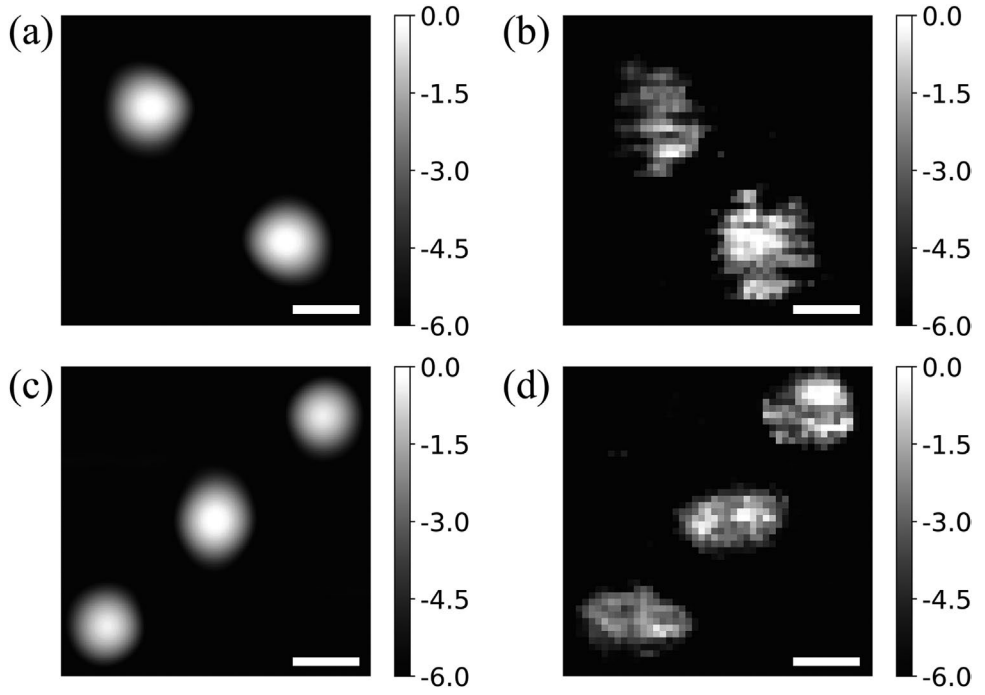

Figure 8. The characterization of multiplexed holograms and comparison with simulation, where (a,c) are the simulation results of two dots and three dots when radii of curvature are $R1 = 35$ mm and $R2 = -100$ mm, and (b,d) are the corresponding experimental results. (a,c) are normalized to the maximum value while (b,d) are normalized to the peak power. The units for simulation and experimental results are in dB. The scale bar is the same for each figure, and it represents 20 mm.

In the visible range, the same number of pixels (with typical periodicity of 400 nm) would cover an area of 500 µm. Therefore, it would be possible to encode several independent images on a holographic metasurface wrapped around a microscopic object extending over several millimeters, provided that one would have knowledge of the shape of the target with an accuracy comparable with that of the wavelength.

5. Conclusion

In conclusion, we have presented the design, fabrication, and characterization of large and flexible holographic metasurfaces, operating at 94 GHz, encoding two independent holographic images which can be obtained for different curvatures of the metasurface. This result will allow a new class of mechanically enabled holographic metasurfaces, for applications in electromagnetic antennas, radar, optomechanical sensors, and actuators.

Supporting Information

Supporting Information is available from the Wiley Online Library or from the author.

Acknowledgements

A.D.F. was supported by the European Research Council (ERC) under the European Union Horizon 2020 research and innovation program (Grant Agreement No. 819346). S.H. acknowledges the Royal Society and TATA for financial support through grant URF\R\211033. S.A.S. acknowledges support from the EPSRC (EP/V029975/1).

Conflict of Interest

The authors declare no conflict of interest.

Data Availability Statement

The data that support the findings of this study are openly available at https://doi.org/10.17630/628402b5-d606-4208-afa2-e59a36355051.[53]

Keywords

conformable metasurfaces, holographic matasurfaces, shape-dependent holograms

Received: November 30, 2022
Revised: January 6, 2023
Published online:

[1] N. Yu, P. Genevet, M. A. Kats, F. Aieta, J.-P. Tetienne, F. Capasso, Z. Gaburro, *Science* **2011**, *334*, 333.
[2] N. Yu, F. Capasso, *Nat. Mater.* **2014**, *13*, 139.
[3] G. Zheng, H. Mühlenbernd, M. Kenney, G. Li, T. Zentgraf, S. Zhang, *Nat. Nanotechnol.* **2015**, *10*, 308.
[4] D. Hu, X. Wang, S. Feng, J. Ye, W. Sun, Q. Kan, P. J. Klar, Y. Zhang, *Adv. Opt. Mater.* **2013**, *1*, 186.
[5] J. Gollub, O. Yurduseven, K. P. Trofatter, D. Arnitz, M. F Imani, T. Sleasman, M. Boyarsky, A. Rose, A. Pedross-Engel, H. Odabasi, et al., *Sci. Rep.* **2017**, *7*, 42650.
[6] J. Burch, J. Ma, R. Hunter, S. Schulz, D. Robertson, G. Smith, J. Wang, A. Di Falco, *Appl. Phys. Lett.* **2019**, *115*, 021104.
[7] J. Hunt, T. Driscoll, A. Mrozack, G. Lipworth, M. Reynolds, D. Brady, D. R. Smith, *Science* **2013**, *339*, 310.
[8] Z. Zhou, J. Li, R. Su, B. Yao, H. Fang, K. Li, L. Zhou, J. Liu, D. Stellinga, C. P. Reardon, T. F. Krauss, X. Wang, *ACS Photonics* **2017**, *4*, 544.
[9] X. Fu, F. Yang, C. Liu, X. Wu, T. J. Cui, *Adv. Opt. Mater.* **2020**, *8*, 1900628.
[10] P. Berini, *ACS Photonics* **2022**, *9*, 2204.
[11] T. Li, X. Xu, B. Fu, S. Wang, B. Li, Z. Wang, S. Zhu, *Photonics Res.* **2021**, *9*, 1062.
[12] X. Ni, A. V. Kildishev, V. M. Shalaev, *Nat. Commun.* **2013**, *4*, 2807.
[13] W. Wan, J. Gao, X. Yang, *ACS Nano* **2016**, *10*, 10671.
[14] Q. Jiang, G. Jin, L. Cao, *Adv. Opt. Photonics* **2019**, *11*, 518.
[15] G. Shang, Z. Wang, H. Li, K. Zhang, Q. Wu, S. N. Burokur, X. Ding, *Photonics* **2021**, *8*, 135.
[16] Y. Hu, L. Li, Y. Wang, M. Meng, L. Jin, X. Luo, Y. Chen, X. Li, S. Xiao, H. Wang, Y. Luo, C.-W. Qiu, H. Duan, *Nano Lett.* **2019**, *20*, 994.
[17] Y. Hu, X. Luo, Y. Chen, Q. Liu, X. Li, Y. Wang, N. Liu, H. Duan, *Light: Sci. Appl.* **2019**, *8*, 86.
[18] M. Khorasaninejad, W. T. Chen, R. C. Devlin, J. Oh, A. Y. Zhu, F. Capasso, *Science* **2016**, *352*, 1190.
[19] H. Liang, Q. Lin, X. Xie, Q. Sun, Y. Wang, L. Zhou, L. Liu, X. Yu, J. Zhou, T. F. Krauss, J. Li, *Nano Lett.* **2018**, *18*, 4460.
[20] R. J. Lin, V.-C. Su, S. Wang, M. K. Chen, T. L. Chung, Y. H. Chen, H. Y. Kuo, J.-W. Chen, J. Chen, Y.-T. Huang, J.-H. Wang, C. H. Chu, P. C. Wu, T. Li, Z. Wang, S. Zhu, D. P. Tsai, *Nat. Nanotechnol.* **2019**, *14*, 227.
[21] H. Zuo, D.-Y. Choi, X. Gai, P. Ma, L. Xu, D. N. Neshev, B. Zhang, B. Luther-Davies, *Adv. Opt. Mater.* **2017**, *5*, 1700585.
[22] J.-H. Song, J. van de Groep, S. J. Kim, M. L. Brongersma, *Nat. Nanotechnol.* **2021**, *16*, 1224.
[23] X. Meng, R. Liu, H. Chu, R. Peng, M. Wang, Y. Hao, Y. Lai, *Phys. Rev. Appl.* **2022**, *17*, 064027.
[24] J. Li, S. Kamin, G. Zheng, F. Neubrech, S. Zhang, N. Liu, *Sci. Adv.* **2018**, *4*, eaar6768.
[25] X. Fang, H. Ren, M. Gu, *Nat. Photonics* **2020**, *14*, 102.
[26] H. Zhou, B. Sain, Y. Wang, C. Schlickriede, R. Zhao, X. Zhang, Q. Wei, X. Li, L. Huang, T. Zentgraf, *ACS Nano* **2020**, *14*, 5553.
[27] S. M. Kamali, E. Arbabi, A. Arbabi, Y. Horie, M. Faraji-Dana, A. Faraon, *Phys. Rev. X* **2017**, *7*, 041056.
[28] A. Leitis, A. Tittl, M. Liu, B. H. Lee, M. B. Gu, Y. S. Kivshar, H. Altug, *Sci. Adv.* **2019**, *5*, eaaw2871.
[29] J. Tang, Z. Li, S. Wan, Z. Wang, C. Wan, C. Dai, Z. Li, *ACS Appl. Mater. Interfaces* **2021**, *13*, 38623.
[30] Z. Tao, X. Chen, H. Jiang, C. Zhang, S. Liu, *J. Opt.* **2017**, *19*, 105102.
[31] W. T. Chen, K.-Y. Yang, C.-M. Wang, Y.-W. Huang, G. Sun, I.-D. Chiang, C. Y. Liao, W.-L. Hsu, H. T. Lin, S. Sun, L. Zhou, A. Q. Liu, D. P. Tsai, *Nano Lett.* **2014**, *14*, 225.
[32] Q. Song, A. Baroni, R. Sawant, P. Ni, V. Brandli, S. Chenot, S. Vézian, B. Damilano, P. de Mierry, S. Khadir, P. Ferrand, P. Genevet, *Nat. Commun.* **2020**, *11*, 2651.
[33] H. Ren, G. Briere, X. Fang, P. Ni, R. Sawant, S. Héron, S. Chenot, S. Vézian, B. Damilano, V. Brändli, S. A. Maier, P. Genevet, *Nat. Commun.* **2019**, *10*, 2986.
[34] Y. Li, X. Li, L. Chen, M. Pu, J. Jin, M. Hong, X. Luo, *Adv. Opt. Mater.* **2017**, *5*, 1600502.

[35] K. Zhang, Y. Yuan, X. Ding, H. Li, B. Ratni, Q. Wu, J. Liu, S. N. Burokur, J. Tan, *Laser Photonics Rev.* **2021**, *15*, 2000351.
[36] D. Wen, F. Yue, G. Li, G. Zheng, K. Chan, S. Chen, M. Chen, K. F. Li, P. W. H. Wong, K. W. Cheah, E. Y. B. Pun, S. Zhang, X. Chen, *Nat. Commun.* **2015**, *6*, 8241.
[37] X. Luo, Y. Hu, X. Li, Y. Jiang, Y. Wang, P. Dai, Q. Liu, Z. Shu, H. Duan, *Adv. Opt. Mater.* **2020**, *8*, 1902020.
[38] T. Zhou, J. Du, Y. Liu, X. Zang, *Opt. Lett.* **2020**, *45*, 463.
[39] E. Arbabi, A. Arbabi, S. M. Kamali, Y. Horie, A. Faraon, *Sci. Rep.* **2016**, *6*, 32803.
[40] W. Ye, F. Zeuner, X. Li, B. Reineke, S. He, C.-W. Qiu, J. Liu, Y. Wang, S. Zhang, T. Zentgraf, *Nat. Commun.* **2016**, *7*, 11930.
[41] H. Cai, J. A. Dolan, G. S. Gordon, T. Chung, D. López, *ACS Photonics* **2021**, *8*, 2581.
[42] B. Xiong, Y. Xu, J. Wang, L. Li, L. Deng, F. Cheng, R.-W. Peng, M. Wang, Y. Liu, *Adv. Mater.* **2021**, *33*, 2005864.
[43] L. Yan, J. Xiao, T. Plaskocinski, M. Biabanifard, S. Persheyev, M. Askari, A. Di Falco, *Opt. Express* **2022**, *30*, 19145.
[44] J. Burch, D. Wen, X. Chen, A. Di Falco, *Sci. Rep.* **2017**, *7*, 4520.
[45] J. Burch, A. Di Falco, *ACS Photonics* **2018**, *5*, 1762.
[46] S. M. Kamali, A. Arbabi, E. Arbabi, Y. Horie, A. Faraon, *Nat. Commun.* **2016**, *7*, 13682.
[47] H.-S. Ee, R. Agarwal, *Nano Lett.* **2016**, *16*, 2818.
[48] S. C. Malek, H.-S. Ee, R. Agarwal, *Nano Lett.* **2017**, *17*, 3641.
[49] R. W. Gerchberg, *Optik* **1972**, *35*, 237.
[50] J. A. Veerman, J. J. Rusch, H. P. Urbach, *J. Opt. Soc. Am. A* **2005**, *22*, 636.
[51] J. Burch, A. Di Falco, *Photonics* **2019**, *6*, 8.
[52] X. Li, C. Rizza, S. A. Schulz, A. Ciattoni, A. Di Falco, *APL Photonics* **2019**, *4*, 056107.
[53] J. Xiao, R. I. Hunter, D. Robertson, G. M. Smith, S. Horsley, S. A. Schulz, A. Di Falco, Shape dependent conformable holographic metasurfaces (Dataset), **2022**, University of St Andrews, https://doi.org/10.17630/628402b5-d606-4208-afa2-e59a36355051 (accessed: January 2023).